Supporting Information:

Impedance-tuned microwave loop for fast, homogeneous Rabi oscillations of a dense ensemble of NV-diamond electronic spins

Han Sae Jung[1,‡], Johannes Cremer[2,‡], Aoyang Zhang[1,3,‡], Shuhao Fan[1], Sangha Kim[1], Guang Yang[1], Ronald L. Walsworth[2,4,5,6,*], and Donhee Ham[1,*]

[1]John A. Paulson School of Engineering and Applied Sciences, Harvard University, Cambridge, MA 02138, USA.
[2]Quantum Technology Center, University of Maryland, College Park, MD 20742, USA
[3]School of Integrated Circuits, Tsinghua University, Haidian District, Beijing 100084, China
[4]Department of Physics, University of Maryland, College Park, MD 20742, USA
[5]Joint Quantum Institute, University of Maryland, College Park, MD 20742, USA
[6]Department of Electrical and Computer Engineering, University of Maryland, College Park, MD 20742, USA
[‡]These authors contributed equally to this work.
*Corresponding author. Email: donhee@seas.harvard.edu, walsworth@umd.edu

This PDF file includes:

METHODS

Chip packaging

To package the chip (fabricated from a foundry), we first glue the chip's backside, which has a 10-µm thick gold layer, to the on-PCB gold plane via conductive silver epoxy; the on-PCB gold plane is internally connected to the on-PCB microstrip ground plane. Then, the two bond pads of the 3-turn loop are wire-bonded to the on-PCB microstrip signal lines. The diamond sample, which is custom-fabricated from Element Six using chemical vapor deposition (CVD), has NV centers embedded on one of its surfaces down to 10-µm depth, and is placed on top of the loop such that the loop is completely covered by the NV-embedded diamond surface. The diamond is glued to the chip by dropping PDMS on its edges and letting the PDMS cure at 80°C by placing the PCB on a hot plate for 15 min.

Optically detected magnetic resonance (ODMR) measurement

A microwave (MW) pulse of 20 µs duration is applied at the same time as an acousto-optic modulator (AOM) pulse (i.e., 532 nm green laser pulse) of 40 µs duration. A DAQ readout pulse of 1 µs duration is applied twice: 2 µs before the end of the MW pulse (i.e., at the 18 µs mark) and 2 µs before the end of the AOM pulse (i.e., at the 38 µs mark). The second readout, which happens in the absence of a MW pulse, serves as a reference readout; the spins are polarized at the $m_s = 0$ state, at which the red NV photoluminescence (PL) emission is at maximum. The PL contrast is calculated by comparing the signal readout (i.e., first readout) to the reference readout (i.e., second readout): $I_{contrast} = I_{sig} / I_{ref}$. This measurement is repeated for a range of different excitation frequencies of the MW pulse and averaged over 500 measurements. ODMR is observed when the PL contrast dips as the excitation frequency matches f_0.

To change f_0 as well as the DC magnet field B_0 alignment to one of the four NV axes, a permanent magnet attached to a motorized stage (Figure S2) is moved linearly in three dimensions while monitoring the ODMR spectrum. NV-centers within an ensemble are typically aligned in equal proportion along all four symmetry axes with the diamond crystal host. An external static (bias) B_0 field has a vector projection on all four axes, which results in multiple small PL contrast dips in the ODMR spectrum. A total of $4 \times 2 = 8$ PL dips are possible in the ODMR spectrum (with sub-structure to each PL dip arising from hyperfine splitting), corresponding to the projections of B_0 on the four NV axes and the $m_s = 0$ to $m_s = +1$ and $m_s = 0$ to $m_s = -1$ electronic spin resonance (ESR) transitions. When B_0 is aligned to one of the four NV axes, we observe one sharp large contrast PL dip for each ESR transition (corresponding to the NV axis aligned with B_0) and three small contrast PL dips for each ESR transition, corresponding to the vector projections of B_0 onto the remaining three NV axes.

Rabi oscillation measurement

A MW pulse of a varying duration is applied at f_0, determined from the ODMR measurement. An AOM pulse of 100 µs duration is applied 1 µs after the end of the MW pulse. A DAQ readout pulse of 1 µs duration is applied 0.5 µs after the start of the AOM pulse. The long AOM pulse duration remaining after the end of the DAQ pulse serves to re-initialize the NV spin to the $m_s = 0$ state before applying the next MW pulse of a different duration. The measurement is repeated for a range of different MW pulse durations and averaged over 500 measurements. How the two levels (m_s = 0 state and either the m_s = +1 state or the m_s = -1 state) are populated depends on the MW pulse duration, which controls the extent of the Rabi oscillation. This dependence is captured by the NV PL contrast plotted as a function of the MW pulse duration, showing the Rabi oscillation dynamics.

Rabi frequency mapping

To determine the microwave field B_1 homogeneity within the 3-turn loop, we map the NV ensemble Rabi frequency f_1, which is directly proportional to the B_1 magnitude. We measure f_1 across a 280 µm × 280 µm area surrounding the innermost turn of the 3-turn loop using a 5-µm diameter laser spot and a 10-µm pixel pitch**.** The loop's interior is scanned using a motorized stage by moving the chip stage with respect to the fixed laser spot location.

Coherently averaged synchronized readout (CASR) detection of an RF signal

To detect a f_{signal} = 29.992 MHz RF signal from a test coil using CASR, an XY8-6 sequence is applied to the NV ensemble with a central frequency $f_{\text{casr}} \approx 30$ MHz (with $\tau = 1/(2f_{\text{casr}})$ being the delay between π pulses). With a 2 µs delay after the XY8-6 sequence ends, an AOM pulse of green laser light of 20 µs duration is applied. With a 1.2 µs delay time after the AOM pulse begins, a DAQ readout pulse of 1 µs duration is applied to measure the NV PL. With a 1 µs delay time after the AOM pulse ends, the next XY8-6 sequence begins. This procedure is repeated until the measurement time reaches 1 s. The frequency of the measured NV PL variation, which is frequency-down-converted from the RF signal by the CASR protocol, is expected to be equal to the absolute difference between f_{casr} and f_{signal}: $\delta f = f_{\text{signal}} - f_{\text{casr}} \approx |30\text{ MHz} - 29.992\text{ MHz}| \approx 8$ kHz. The Fourier transform of the measured CASR PL signal shows a single peak at this expected frequency, with a small difference within the 1 ppm error of the signal generator (Rigol DG 1032). The spectral resolution of a CASR measurement is given by the full width at half maximum of the signal peak in the Fourier transform. The Fourier limit to this spectral resolution is set by the reciprocal of the measurement time. CASR detection of the same RF signal is also performed for measurements times of 10 s and 100s, with spectral resolution given by the Fourier limit for the 1 s and 10 s measurements, and by about 0.05 Hz for the 100s measurement, limited by drift in the system, *i.e.*, stability of the timing source used to control the CASR protocol. (Figure S11).

Work	Single NV vs. Ensemble	Location	ESR Frequency f_0 (GHz)	Rabi Frequency f_1 (MHz)	f_1 / f_0	MW Power (W)	Driving Efficiency (MHz/$\sqrt{\text{W}}$)
This work	Ensemble	Center	2.55 (optimal)	136.3	5.3×10^{-2}	34.8	23.1
Ref. 4	Ensemble	Center	2.87	14.3	5.0×10^{-3}	0.5	20.2
Ref. 5	Ensemble	Center	2.82	4.6	1.6×10^{-3}	1.0	4.6
Ref. 7	Ensemble	Center	2.67	7.9	3.0×10^{-3}	4.0	3.9
Ref. 3	Single	Close to trace	0.49	440	9.0×10^{-1}	0.4	697.4
Ref. 6	Ensemble	At trace	2.73	165	6.0×10^{-2}	3.4	89.6

Table S1. Comparison of device used in present work to several other works in the literature, both those that measure NV Rabi oscillations at the center of a loop (lower Rabi frequency and better microwave field spatial homogeneity) and directly at or near the metal trace (higher Rabi frequency and poorer homogeneity).

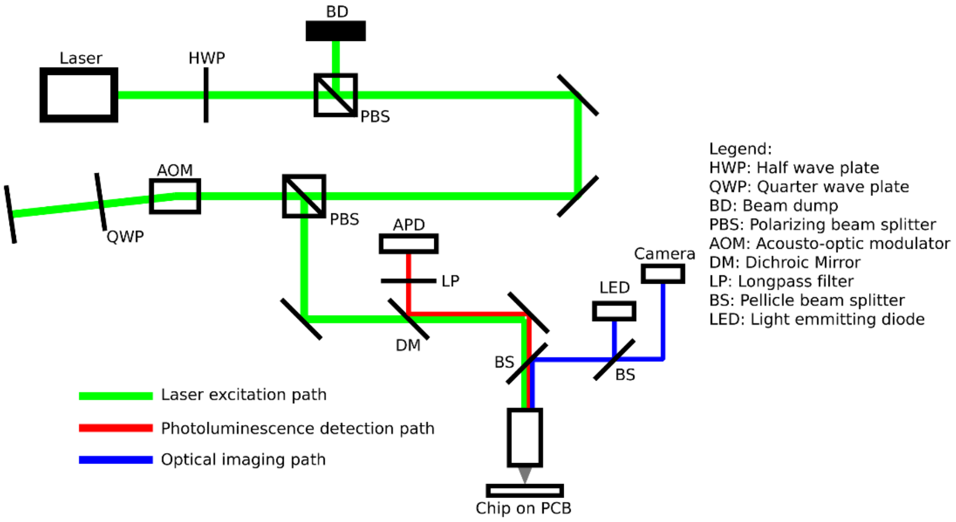

Figure S1. Optical setup for NV excitation and detection. Light from a 532nm laser (Lighthouse Sprout) is polarized with a half wave plate (HWP) and a polarizing beam splitter cube (PBS). It is pulsed using an acousto-optic modulator (AOM) in a double pass configuration consisting of a second PBS and a quarter wave plate (QWP). The pulsed light is focused on the chip with a 20× microscope objective (Mitutoyo Plan Apo Infinity Corrected LWD). NV photoluminescence (PL, red) is collected through the same objective and focused onto an avalanche photodiode (APD, Thorlabs APD130A) with a dichroic mirror (DM) and through a long-pass filter (LP). An additional imaging pathway (blue) based on a 450 nm LED allows precise positioning of the laser spot on the chip. The first pellicle beam splitter (BS) is mounted on a flip mount and is removed during PL measurements. The sample is mounted on a 3-axis stage for scanning and focus adjustment.

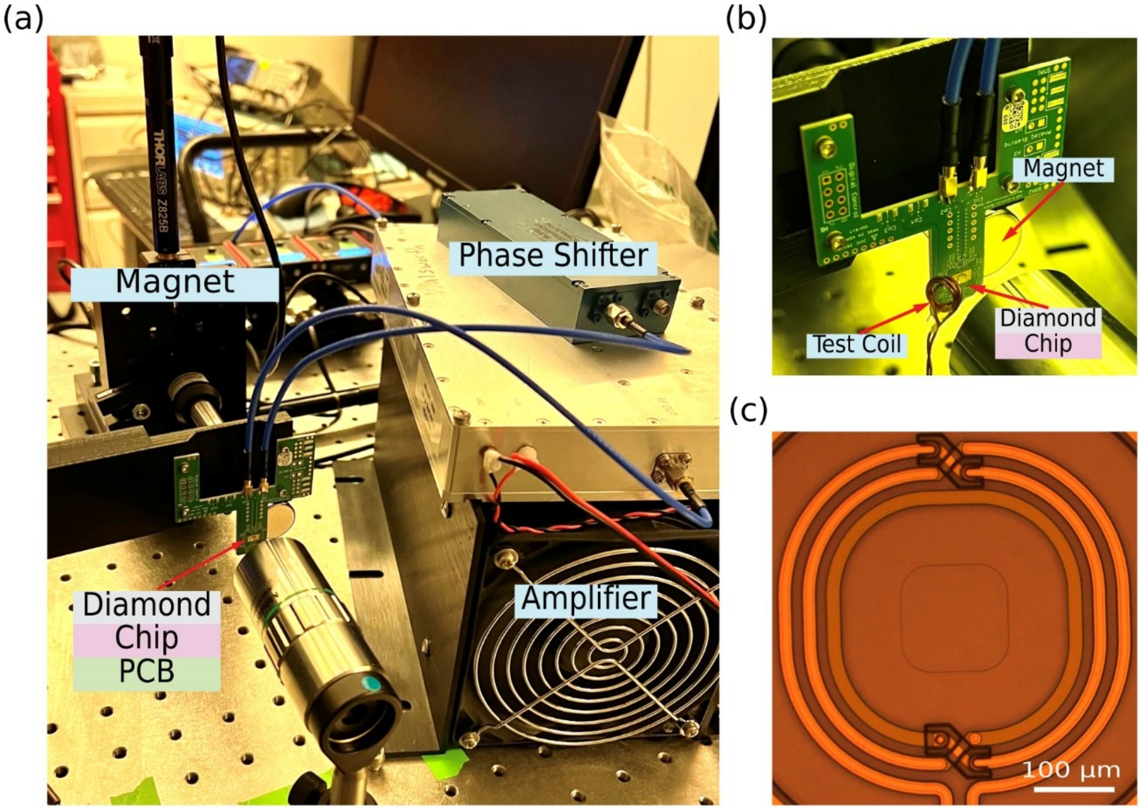

Figure S2. Experimental setup. (a) The setup showing the device (the chip with the 3-turn loop plus diamond) on a PCB, the magnet, the phase shifter, and the power amplifier. (b) Close-up view of the device on the PCB, during a CASR detection of an RF signal from a test coil. (c) Optical image of the 3-turn loop. The metal trace is 17 µm wide, with the gap between the metal traces being 13 µm. The diameters (center-to-center distance between the metal traces) of the innermost loop, the second loop, and the outermost loop are 300 µm, 360 µm, and 420 µm, respectively.

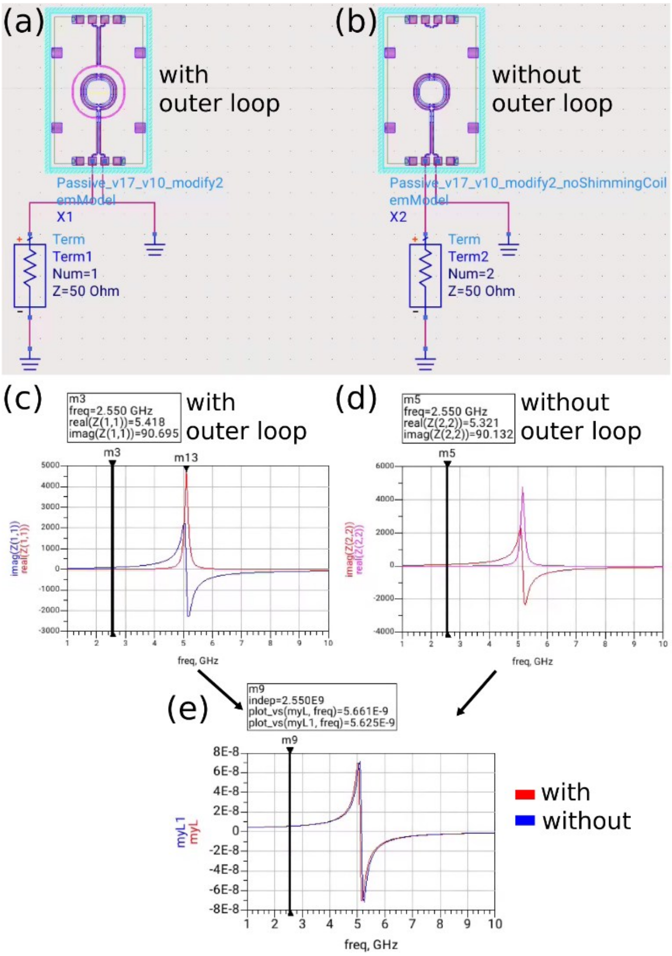

Figure S3. Simulation of the 3-turn primary loop with and without the open-circuited outer secondary loop. (a, b) s_{11} simulation setup of the 3-turn loop with and without the outer loop. (c, d) Real and imaginary parts of the loop impedance Z_L vs. excitation frequency f_0, extracted from the simulated s_{11} in both cases, showing nearly identical results. For example, at 2.55 GHz, $Z_L \approx 5.4 + 90.7i\ \Omega$ with the outer loop and $Z_L \approx 5.3 + 90.1i\ \Omega$ without, and their corresponding quality factors are $Q \approx 16.8$ and $Q \approx 17.0$. The simulation results also show that the self-resonance frequency of the primary loop is $f_{SRF} \approx 5.1$ GHz in both cases. For the loop circuit model shown in Figure 1c, $Z_L = (R_L + i\omega_0 L_L)||(i\omega_0 C_L)^{-1} \equiv R_{\mathrm{eff}} + i\omega_0 L_{eff}$ where $L_{eff} \approx L_L[1-(\omega_0/\omega_{SRF})^2]^{-1}$ and $R_{\mathrm{eff}} \approx R_L[1-(\omega_0/\omega_{SRF})^2]^{-2}$ ($\omega_0 = 2\pi f_0$, $\omega_{SRF} = 2\pi f_{SRF}$). Comparing these expressions with the simulated Z_L values at 2.55 GHz gives $L_L \approx 4.25$ nH and $R_L \approx 3.04\ \Omega$ with the outer loop, and $L_L \approx 4.22$ nH and $R_L \approx 2.98\ \Omega$ without. From $f_{SRF} = (2\pi)^{-1}(L_L C_L)^{-1/2} \approx 5.1$ GHz, we then obtain $C_L \approx 0.229$ pF with the outer loop and $C_L \approx 0.231$ pF without. As seen, the open-circuited outer loop has negligible effect on the primary loop parameters. (e) The imaginary parts of (c) and (d), rescaled by $1/(\omega_0)$, are overlayed to further illustrate this negligible difference; since $Z_L = R_{\mathrm{eff}} + i\omega_0 L_{eff}$, these curves represent L_{eff} with and without the outer loop.

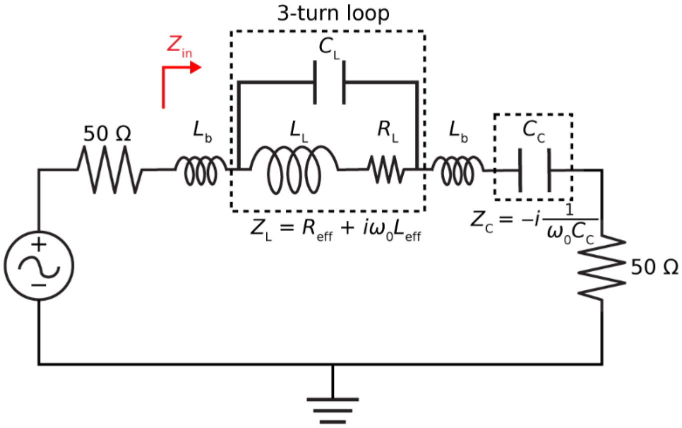

Figure S4. Circuit model of the full microwave signal path when the open-terminated phase shifter in Figure 1c is replaced by a 50-Ω termination.

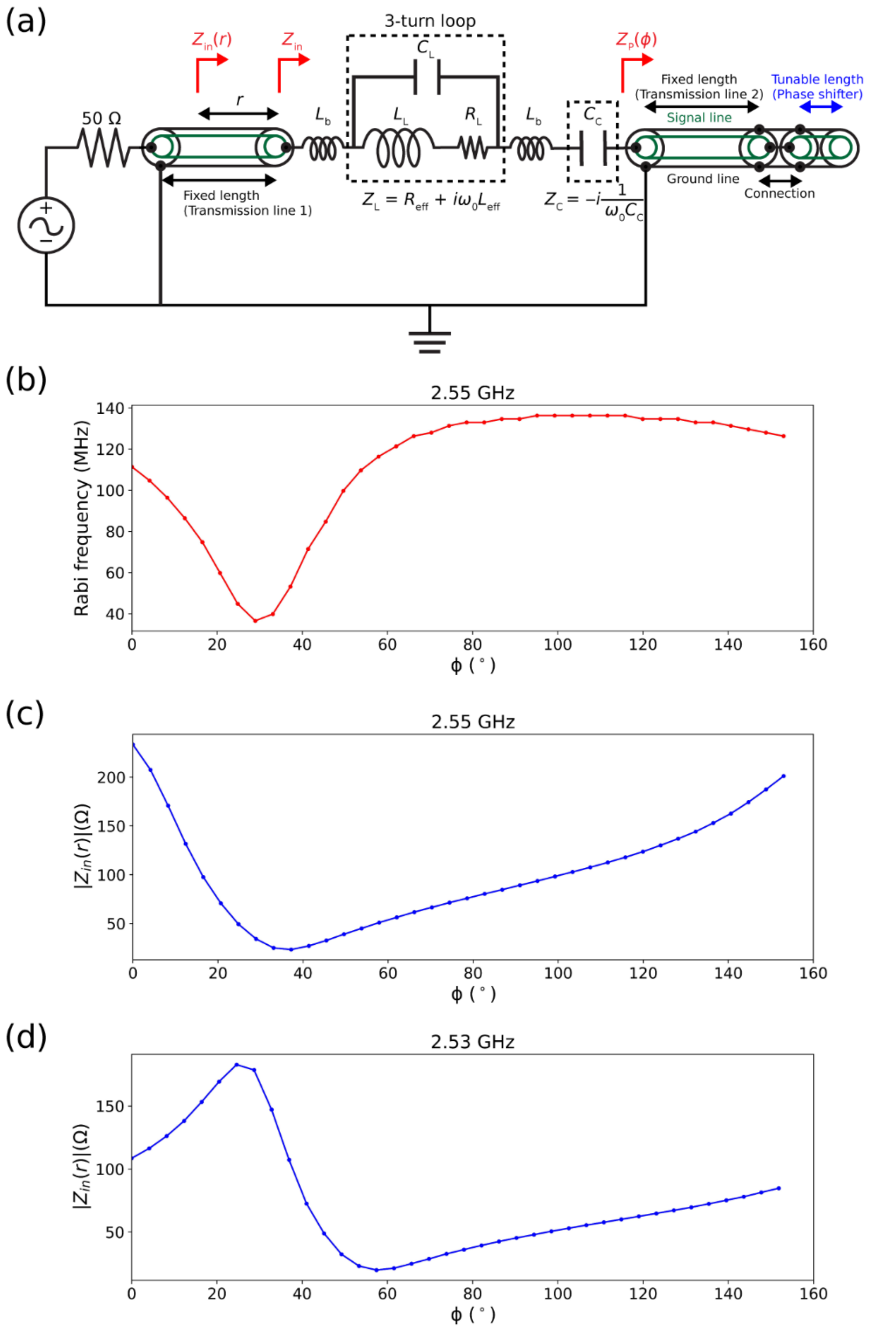

Figure S5. Impedance analysis via 1-port *s*-parameter measurement. (a) Electrical model of the device and measurement configuration. Unlike Figure 1c of the main text, Transmission line 1 is shown explicitly. We measure 1-port *s*-parameter (s_{11}, the reflection coefficient) as a function of the phase delay ϕ at $f_0 = 2.55$ GHz. Calibration standards for the *s*-parameter measurement cannot be placed at the junction between Transmission line 1 and the device (since the microstrip of Transmission line 1 is fixed on the PCB), so a standard calibration is not possible. As a result, the reference plane for s_{11} lies at an unknown but fixed distance r along Transmission line 1 from the device, meaning we obtain an input impedance at that position, $Z_{in}(r)$, rather than the true device input impedance Z_{in}. $Z_{in}(r)$ is extracted from the measured s_{11} via $Z_{in}(r) = Z_0 \times (1 + s_{11}) / (1 - s_{11})$

with $Z_0 = 50\ \Omega$. (b) Measured Rabi frequency f_1 versus ϕ at $f_0 = 2.55$ GHz (reproduced from Figure 2a of the main text). (c) $|Z_{in}(r)|$ versus ϕ at $f_0 = 2.55$ GHz, obtained as explained in (a). (d) Same as (c), but at $f_0 = 2.53$ GHz, which reveals the $|Z_{in}(r)|$ maximum not visible in (c) within the accessible ϕ range.

To interpret these results, we recall the relationship between $Z_{in}(r)$ and Z_{in}: $Z_{in}(r) = Z_0 \times [Z_{in} + iZ_0 \tan(\omega_0 r/v)] \times [Z_0 + iZ_{in} \tan(\omega_0 r/v)]^{-1}$ where v is the microwave propagation velocity on Transmission line 1 (Since Transmission line 1 consists of a coaxial cable and a microstrip and the microwave velocity differs in each, the true relation between $Z_{in}(r)$ and Z_{in} is even more complex, which becomes even more compounded if loss is included. The relationship above is to capture the essence in a simpler form). Due to this nonlinear transformation, the extrema of $|Z_{in}(r)|$ generally do not coincide with those of Z_{in}, either in their ϕ positions or in their magnitudes. f_1 reaches its maximum and minimum when $|Z_{in}|$ is minimized and maximized, respectively. However, because the measurement yields $|Z_{in}(r)|$ rather than $|Z_{in}|$, the ϕ positions of the f_1 maximum and minimum in (b) do not align with the ϕ positions of the minimum and maximum of $|Z_{in}(r)|$ in (c) (as mentioned above, at 2.55 GHz in (c), the $|Z_{in}(r)|$ maximum is not visible within the accessible ϕ range; however, its existence is revealed by slightly changing the excitation frequency to 2.53 GHz, as shown in (d), since the excitation frequency directly influences $|Z_{in}(r)|$ through the nonlinear transformation). In summary, while direct measurement of Z_{in}, rather than $Z_{in}(r)$, would provide the clearest correspondence between the extrema of f_1 and $|Z_{in}|$, such measurement is not feasible due to calibration constraints. Nevertheless, the observed extrema in $|Z_{in}(r)|$ indicate the underlying extrema of $|Z_{in}|$ that govern the f_1 extrema, even though their ϕ positions and magnitudes do not coincide due to the nonlinear relationship.

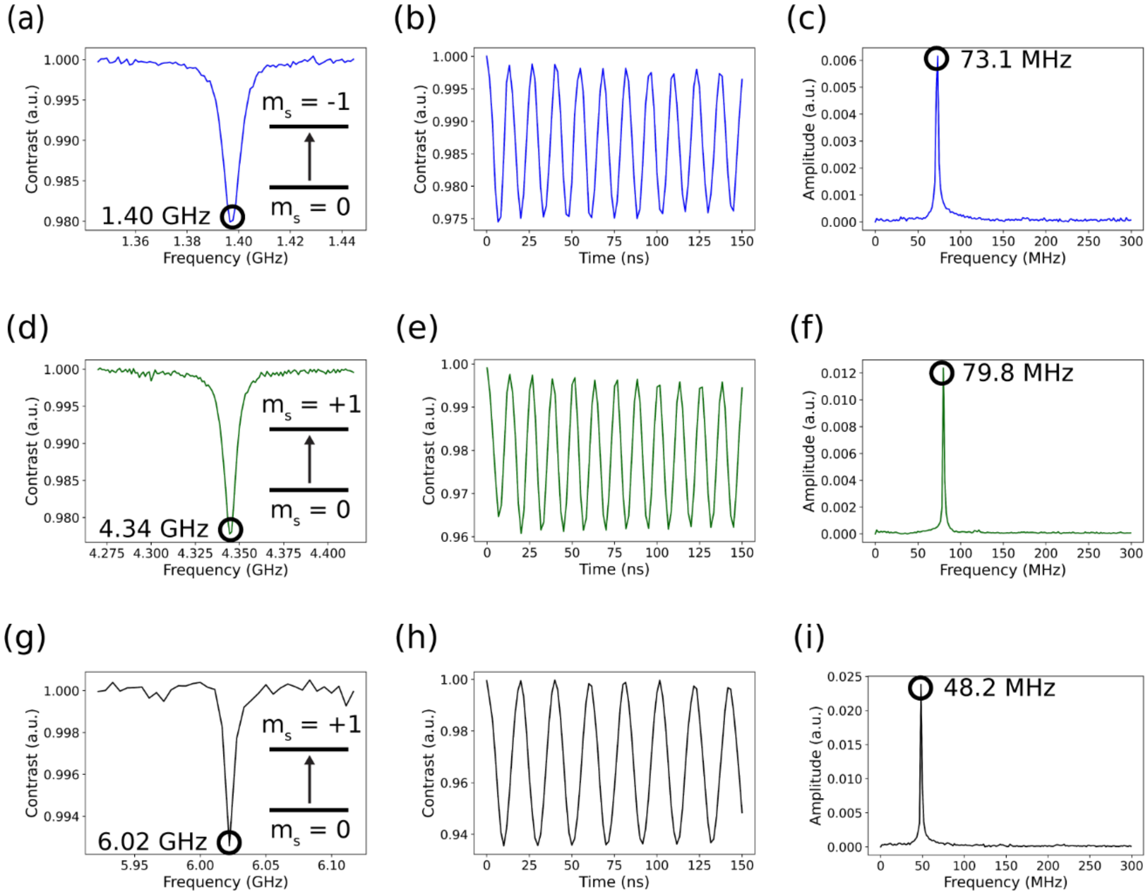

Figure S6. NV ODMR and Rabi oscillation measurements at various f_0 values. (a) ODMR spectrum for the $m_s = 0$ to $m_s = -1$ NV ESR transition at f_0 = 1.40 GHz (B_0 = 526 G). (b) Rabi oscillation measurement using the ESR transition in (a). (c) Fourier transform of the Rabi oscillation measurement in (b), showing a single peak at f_1 = 73.1 MHz. (d) ODMR spectrum of the $m_s = 0$ to $m_s = +1$ NV ESR transition at f_0 = 4.34 GHz (B_0 = 526 G). (e) Rabi oscillation measurement using the ESR transition in (d). (f) Fourier transform of the Rabi oscillation measurement in (e), showing a single peak at f_1 = 79.8 MHz. (g) ODMR spectrum of the $m_s = 0$ to $m_s = +1$ NV ESR transition at f_0 = 6.02 GHz (B_0 = 1125 G). (h) Rabi oscillation measurement using the ESR transition in (g). (i) Fourier transform of the Rabi oscillation trace measurement in (h), showing a single peak at f_1 = 48.2 MHz.

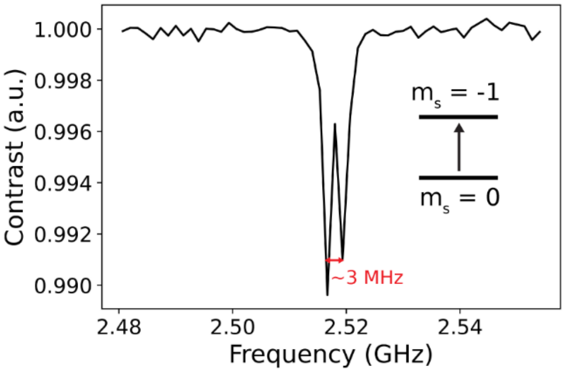

Figure S7. NV ODMR spectrum under low microwave power at f_0 = 2.52 GHz. The two dips correspond to the hyperfine splitting of the NV electron spin with the ^{15}N nuclear spin (our diamond sample is grown with isotopically purified ^{15}N), separated by ~3 MHz. Because this splitting is much smaller than f_1 (*i.e.*, 136.3 MHz), the two corresponding detuned Rabi oscillations cannot be resolved experimentally and instead appear as a single, clean oscillation.

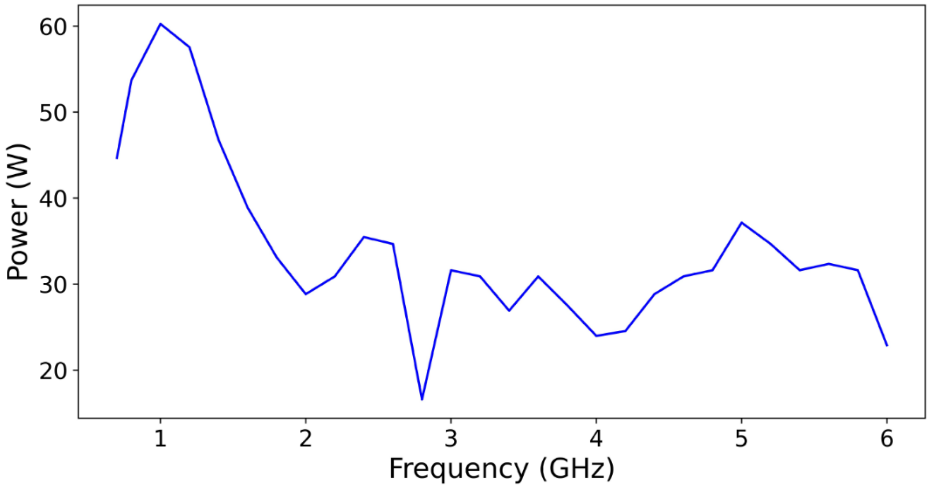

Figure S8. Output power of the Mini-Circuits ZHL-25W-63+ power amplifier as a function of microwave excitation frequency, derived from the vendor's publicly available data set describing the amplifier's saturated power output (shown in dBm in their document) as a function of excitation frequency (see Reference 1 of the Supporting Information).

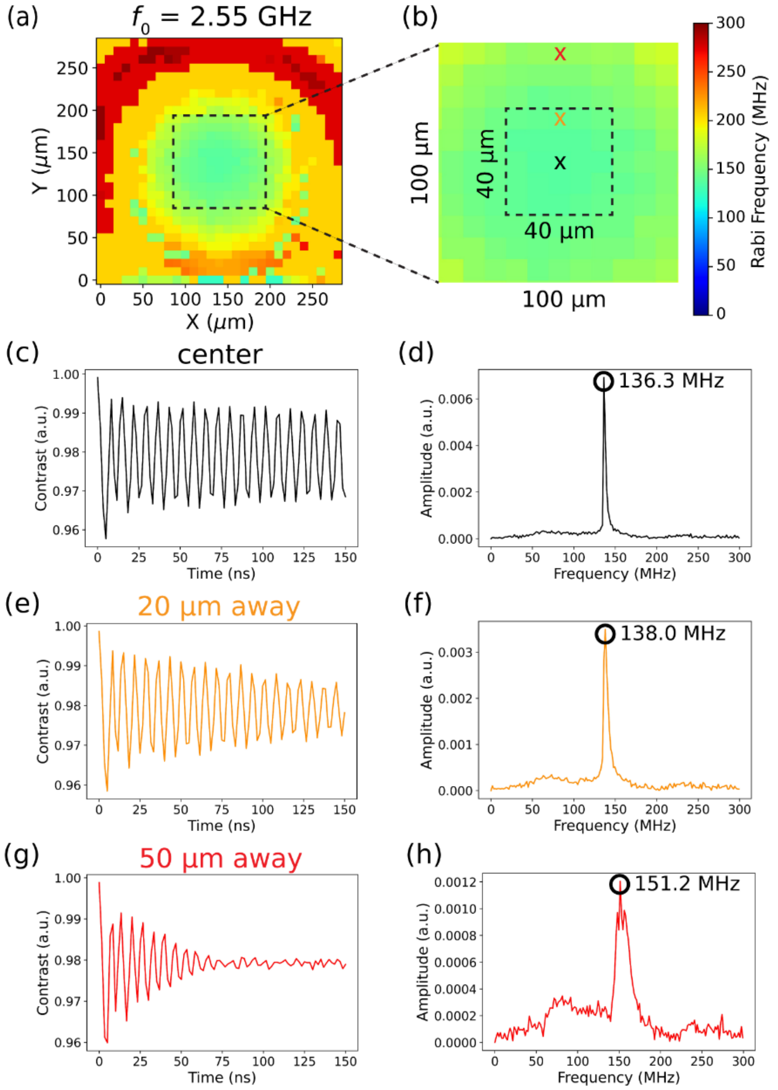

Figure S9. f_1 measurements at varying distances from the center of the 3-turn loop for the NV-measured map of f_1 shown in Figure 3a and Figure 3b at f_0 = 2.55 GHz. (a, b) f_1 map and its close-up view shown in Figure 3a and Figure 3b, respectively. The 100 µm × 100 µm area around the center is denoted by the dashed square in (a). The 40 µm × 40 µm area around the center is denoted by the dashed square in (b). The black, yellow, and red crosses denote the locations that are 0 µm, 20 µm, and 50 µm away from the center, respectively. (c) Rabi oscillation measurement at the center. (d) Fourier transform of the Rabi oscillation measurement in (c), showing a single peak at f_1 = 136.3 MHz. (e) Rabi oscillation measurement at the 20 µm mark. (f) Fourier transform of the Rabi oscillation measurement in (e), showing a single peak at f_1 = 138.0 MHz. (g) Rabi oscillation measurement at the 50 µm mark. (h) Fourier transform of the Rabi oscillation measurement in (g), showing a peak at f_1 = 151.2 MHz. Moving away from the loop center, there is increasing spatial variation in microwave field strength, leading to enhanced damping of observed Rabi oscillations and corresponding broadening of the Fourier transform.

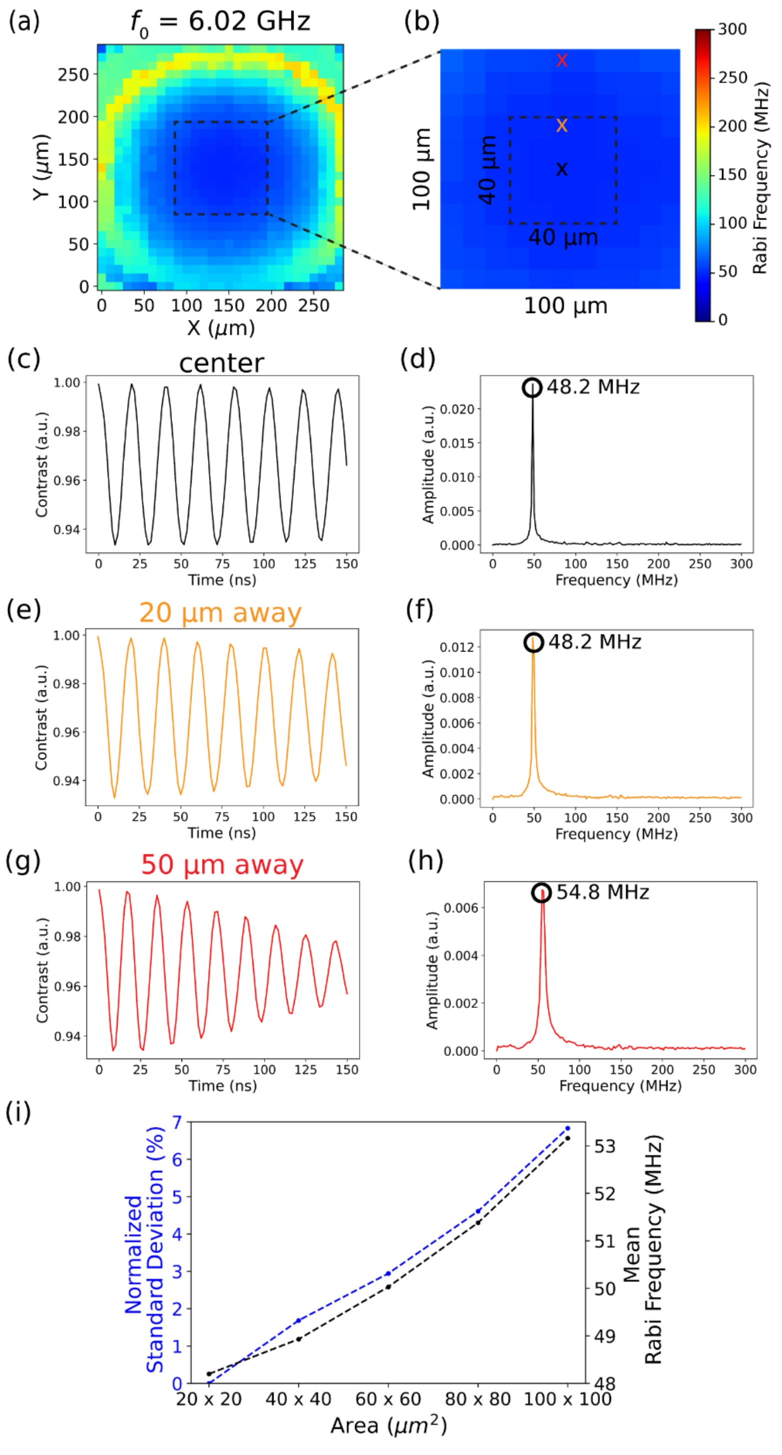

Figure S10. f_1 measurements at varying distances from the center of the 3-turn loop for the NV-measured map of f_1 at f_0 = 6.02 GHz. (a) f_1 map. The 100 μm × 100 μm area around the center is denoted by the dashed square. (b) Close-up view of the 100 μm × 100 μm area shown in (a). The 40 μm × 40 μm area around the center is denoted by the dashed square. The black, yellow, and red crosses denote the locations that are 0 μm, 20 μm, and 50 μm away from the center, respectively. (c) Rabi oscillation measurement at the center. (d) Fourier transform of the Rabi oscillation measurement in (c), showing a single peak at f_1 = 48.2 MHz. (e) Rabi oscillation measurement at the 20 μm mark. (f) Fourier transform of the Rabi oscillation measurement in (e), showing a single peak at f_1 = 48.2 MHz. (g) Rabi oscillation measurement at the 50 μm mark. (h) Fourier transform of the Rabi oscillation measurement in (g), showing a peak at f_1 = 54.8 MHz. As in Figure S9, there is increasing spatial variation in microwave field strength moving away from the loop center, leading to enhanced damping of observed Rabi oscillations and corresponding broadening of the Fourier transform. (i) Mean and normalized standard deviation of f_1 vs. window size centered on the loop center, obtained from the f_1 map in (a). The normalized standard deviation is about 1.7% within the 40 μm × 40 μm region. Although f_0 = 6.02 GHz is above the $f_{\mathrm{SRF}} \approx 5.1$ GHz, the f_1 homogeneity is maintained, but further experimental verification is needed on whether this trend holds in general (*i.e.*, for any $f_0 > f_{\mathrm{SRF}}$).

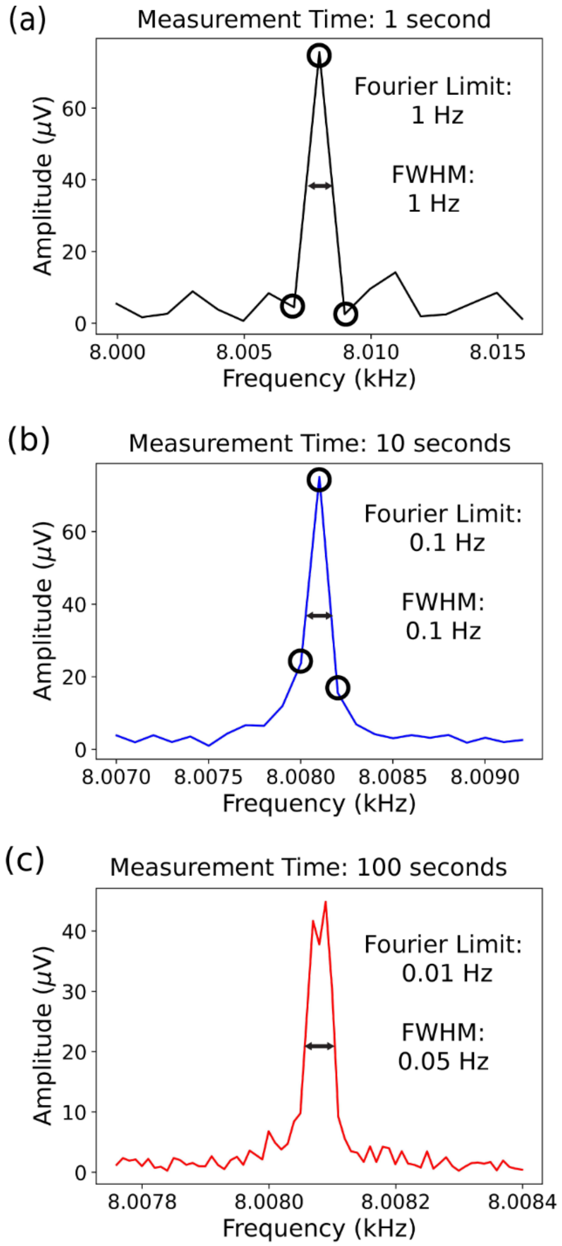

Figure S11. Determination of the spectral resolution for the coherently averaged synchronized readout (CASR) measurement shown in Figure 4 at varying measurement times. (a) Fourier transform for a 1 s CASR measurement. The spectral resolution, determined by the full width at half maximum (FWHM) of the Fourier transform, is set by the Fourier limit, i.e., 1 Hz for a 1 s measurement. (b) Fourier transform for a 10 s CASR measurement. The spectral resolution is again set by the Fourier limit (0.1 Hz). (c) Fourier transform for a 100 s CASR measurement. The spectral resolution is about 0.05 Hz, limited by system drift.

REFERENCES

1. ZHL-25W-63+. *Datasheet*. Mini-Circuits. https://www.minicircuits.com/WebStore/dashboard.html?model=ZHL-25W-63%2B